2012 IEEE/RSJ International Conference on
Intelligent Robots and Systems
October 7-12, 2012. Vilamoura, Algarve, Portugal

Understanding Soft Tissue Behavior for Microlaparoscopic Surface Scan*

Mustafa Suphi Erden, Benoit Rosa, Jerome Szewczyk, and Guillaume Morel, *Member, IEEE*

***Abstract*—This paper presents an approach for understanding the soft tissue behavior in surface contact with a hard object scanning the tissue. The application domain is confocal microlaparoscope imaging, mostly used for imaging the outer surface of the organs in the abdominal cavity. The probe (optic-head) is swept over the tissue to collect sequential images to obtain a large field of view with mosaicing. The problem we address is that the tissue also moves with the probe due to its softness; therefore the resulting mosaic is not in the same shape and dimension as traversed by the probe. Our approach inspires from the finger slip studies and adapts the idea of load-and-slip that explains the movement of the finger when dragged on a hard surface. We propose the concept of loading-distance and perform measurements with in total 84 experiments on beef liver and chicken breast tissues. Our results indicate that the loading-distance can be measured prior to a scan and be used during the scan in order to compensate the movement of the probe. In this way we can have an image-mosaic of the tissue surface in a desired shape.**

I. Introduction

THIS paper presents a first attempt to understand the soft tissue behavior at the contact surface while being scanned with a rigid object for confocal microscopy. Confocal microlaparoscopy is a promising approach for detecting cancer cells on the outside tissues of organs, such as in the abdominal cavity. It is recently used *in vivo* on human body [1]. The microlaparoscope imaging is minimally-invasive, therefore significantly eliminates many of the risks of an open surgery. Microendoscope imaging is also improving with the design of actively controlled endoscopes [2].

There have been different designs of confocal micro imaging of living tissues for microlaparoscopy [3] and microendoscopy [4, 5, 6]. The images obtained typically cover an area of 240×200 μm^2. The smallness of the image size is, on the one hand, because of the necessity of a fine resolution, on the other hand, because the optic lenses and the fiber cable are minimized for minimal invasiveness. An image of such size is not enough for a conclusive diagnostics. A solution to obtain larger scale images is to scan the region of interest and merge the collected images by mosaicing algorithms [7, 8]. The research in [9] demonstrates the applicability of this approach to *in vivo* image-mosaicing on human patients by manually passing the miniprobe over the region of interest and by using the mosaicing algorithm in [10]. Image-mosaicing with confocal microscopy is performed also on human-hand skin by again manually dragging a MEMS based scanner [11] and using the mosaicing algorithm in [12]. Although these studies show the feasibility of image-mosaicing with confocal microscopy, they do not propose an automated way of scanning the tissue for the purpose of collecting sequential images.

In [13] the authors present a wide angle view endoscope which uses two articulated wedge prisms that can be rotated by two motors. The prisms noted to be under construction are 12 mm in diameter, which is quite large for laparoscopic operations. A typical scan for image-mosaicing in laparoscopic operations requires a position precision of up to 50-100 μm for duration of typically one minute. With manual sweeping it is difficult to obtain this precision. Assistive handheld instruments are presented for micro positioning, for intraocular laser surgery [14] and for confocal laser endomicroscopy [15], but they are large to be used in minimally invasive surgery and are not intended for long continuous manipulation through a given trajectory. The motorized surgical microscope presented in [16] enables the surgeon to control the movement of the microscope by index finger movements with a remote controller. Although, this is a semi-automated system, it would be tedious for a surgeon to make the probe follow a proper scan path by finger movements.

A recent study by the latter three authors and colleagues demonstrates a design for automated confocal microlaparoscopic scanner based on hydraulic balloon catheters actuation, mounted inside a 5 mm inner diameter tube [17]. An important issue with such a system is that the surface of the soft tissue deforms under the contact with the probe while scanning. This is because of the friction at the contact surface. Due to the deformation the trajectory of the probe with respect to the tissue surface significantly deviates from the trajectory of the probe with respect to the global reference frame. Therefore, a correction action is required to compensate for the tissue motion and deformation [18].

The question is how to design a proper trajectory of the probe with respect to the global reference frame in order to obtain the desired trajectory of the probe with respect to the tissue surface. In order to answer this question one needs to

*Research funded by OSEO (Maisons-Alfort, France) under the ISI Project PERSEE (number I0911038W).

M.S. Erden was with the Institut des Systèmes Intelligents et de Robotique (ISIR) at Université Pierre et Marie Curie (UPMC), Paris, France. He is now with the LASA Laboratory at the Engineering School of École Polytechnique Fédérale de Lausanne, CH 1015, Switzerland. (corresponding author: + 33 (0) 1 44 27 62 64 ; fax: +33.1.44.27.51.45; e-mail: mustafasuuphi.erden@gmail.com).

B. Rosa, J. Szewczyk, and G. Morel are with ISIR at UPMC, Paris, France (e-mail: {rosa, sz, morel}@isir.upmc.fr).

know how the soft tissue behaves when it is subject to a dragging friction force on the surface. This paper contributes to understanding such tissue behavior by inspiration from finger slip studies, by presenting the results of soft-tissue experiments, and by proposing a quantitative parameter that describes the soft tissue behavior.

Scanning for image collection for image-mosaicing should not be confused with *scanning for image construction*. Almost all laser based micro imaging technologies scan the tissue for image construction, either for illumination with the laser light [19, 20], for light reception from selectively distinguished regions [21], or for both illumination and reception [11]. The probe is stationary during this process. Unlike these, the system presented in [17] and the content of this paper is related to *scanning for image collection*, which refers to moving the probe along the tissue surface to collect images to be used for mosaicing.

In the literature there are various studies about soft tissue modeling [18]. Most of these studies aim at modeling the reaction forces against indentation [22] or pulling with solid instruments [23] and most of them are intended for simulation purposes in virtual environments [24]. The finite-element modeling is a common continuum-based approach for modeling the soft-tissue behavior [24, 25]. The mass-spring model is a discrete approach approximating the continuous tissue structure by a finite set of nodes and massless-springs [24, 26]. None of the above studies dwell upon the behavior of soft tissue under frictional effects. The paper [27] develops a simulation of friction contact with soft tissue for colonoscopy simulator. The model makes use of the idea of stick and slip phases like in our paper. The simulation uses *a priori* known friction coefficients.

Our research inspires from the finger slip studies [28, 29, 30]. As it is reviewed in Section III, these studies point out to the load-slip phenomenon observed in the soft tissue of the finger under the impact of a frictional surface contact. We make use of this idea to explain the behavior of the soft tissue being scanned with a solid object, the probe. The confocal imaging systems and the scanning tool such as in [17] provide very limited space for mounting a force sensor at the distal end. Therefore, our approach of understanding the soft tissue behavior does not make use of force measurements. Rather, we aim at understanding how the tissue acts, by comparing the movement of the tissue with the movement of the probe performing the scan.

II. Experimental Setup

The *ex-vivo* imaging experiments presented in this paper make use of the Cellvizio imaging technology from the Mauna Kea Technologies (Paris, France) [21]. This system performs confocal fluorescence imaging. It constructs images of size 240×200 μm^2 with 1.2 μm lateral and 3 μm axial resolutions at a rate of 12 frames/sec. The excitation wavelength is 488 nm. In our *ex vivo* experiments we apply Acriflavine on the tissue as the fluorescent agent. The system is equipped with the mosaicing algorithm presented in [10, 31]. This is a correlation function based algorithm, designed to account for difficulties typical of *in vivo* tissue imaging, such as motion distortions, irregularly shaped frames, and non-rigid deformations. It can construct a mosaic out of sequentially collected images. The overall confocal-probe consists of a flexible bundle of optical fibers and an optic-head hosting the micro lenses, located at the tip. The outer diameter of the flexible bundle is 1.4 mm. The optic-head is a 12 mm long cylinder with an outer diameter of 2.6 mm. In this paper the word "probe" refers to the optic-head.

(a) (b)

Fig. 1. Experimental setup for soft tissue scans. (a) Left to right: the Stäubli-Robot, the computer controlling the robot, and the computer performing the image acquisition. (b) The soft tissue (beef liver) under the probe attached to the end-effector of the robot.

The *ex-vivo* experiments are performed with the six degrees-of-freedom Stäubli-Robot (Stäubli-TX40) on beef liver and chicken breast purchased from the supermarket (Fig. 1). The robot is commanded to follow a desired trajectory. With our control algorithm the deviation of the robot from a commanded trajectory might be up to around 50 μm. Under the control of the robot the probe is moved on the soft tissue. We name the trajectory of the probe with respect to the global reference frame as the *probe trajectory*. The Cartesian space measurement of the Stäubli-Robot has a nominal precision of 20 μm. Therefore we can assume that our probe trajectory measurements have a precision of up to 20 μm. We pass the position signals of the robot through a low pass filter in order to get rid of the measurement noise. The trajectory of the probe with respect to the tissue surface is named as the *image trajectory*. The image trajectory deviates from the probe trajectory; because the tissue also moves under the impact of the movement of the probe. The image trajectory can be captured by using the motion field vectors obtained by comparing successive images. The imaging algorithm in our Cellvizio system [31] performs this calculation and returns the position difference between the centers of sequential images throughout the scan.

III. Load-Slip Phenomenon on Soft Tissue

It is demonstrated in finger slip studies [28, 29, 30] that when a finger is dragged on a solid surface, the soft tissue experiences two successive phases of movement: loading and slipping. In the loading phase the central part of the tissue remains stuck to the surface. Throughout loading, the drag force at the contact surface remains less than the friction introduced by the sticking regions. The friction force

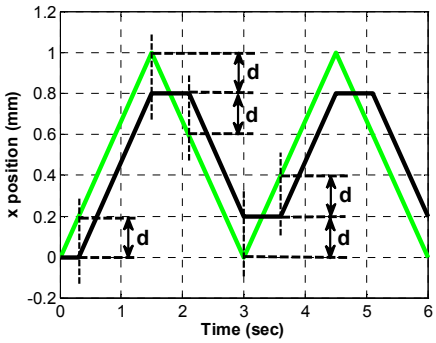

Fig. 2. Ideal soft-tissue behavior according to load-slip phenomenon.

acting on the soft tissue is in the opposite direction of the dragging force. The soft tissue deforms under the impact of the friction force and is loaded with stress. This stress pulls the contact surface in the opposite direction of the friction force. When the most central point starts slipping with the other parts, the finger enters into the slipping phase. In this phase, the drag force is equal to the friction. There is a stationary stress on the soft tissue and it remains throughout the movement in the slipping phase.

The situation of scanning a soft tissue with a solid probe is very similar to the movement of the finger tissue on a solid surface. In the case of the finger, the soft tissue is dragged on solid surface. In the case of the scanning, it is the other way around: the solid probe is dragged on the soft tissue. The stress is accumulated on the surface being scanned, rather than the moving part. When the probe is dragged, up to some point, it does not move with respect to the soft tissue surface; because the contact surface of the tissue sticks to the probe and moves together. This is the loading phase of the scan. In this phase the drag force is less than the friction at the contact surface. Contrary to the case of the finger, the friction force acting on the soft tissue is in the same direction as the dragging force. This friction force results in deformation and loads the tissue with stress: the contact point stretches in the direction of the drag. When the dragging force overcomes the friction, the probe starts moving with respect to the tissue surface. In this way the movement enters into the slipping phase. While the probe is moving, the parts of the soft tissue on which it propagates are constantly loaded and unloaded with stress. Namely, unlike the case of the finger, the stress propagates on the soft tissue with the probe throughout the slipping phase.

When we apply the idea of load-slip phenomenon to the case of a line scan, the ideal behavior would look like in the hypothetical graph in Fig. 2. In this graph the light (green) lines correspond to the position of the probe with respect to the global reference frame and the dark (black) lines correspond to the position of the probe with respect to the surface of the soft tissue. At the very start, the probe moves and loads the tissue; therefore the image does not move. When the probe reaches a distance of d the tissue is fully loaded and enters into the slipping phase. From this point on the image follows the probe with the same speed, with a position lag of distance d, up to the point that the latter stops. At 1.5 sec, the probe stops and starts moving in the opposite

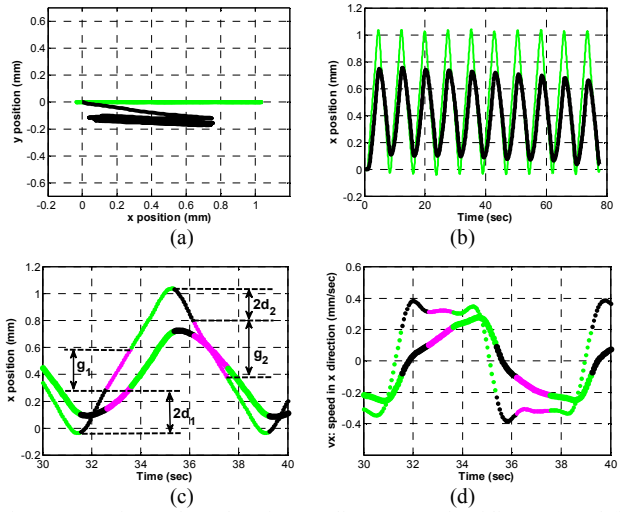

Fig. 3. Experimental results of 1 mm line scan on beef liver. (a) and (b): Light (green) line is the probe trajectory; dark (black) is the image trajectory. (c) The position profile in x-direction; (d) velocity profile in x-direction. In (c) and (d): the thin lines represent the probe movement; the thick lines represent the image movement; light (green) parts represent the slipping phases; dark (black) parts represent the load phases; gray (pink) parts represent the load+slip phases.

direction ($-x$). With the reverse movement of the probe the tissue starts unloading the stress. After the probe moves a distance of d the stress is totally unloaded. At this moment the probe and the image trajectories have the same position value (0.8 mm). The probe goes further in the $-x$ direction and starts loading the tissue in the reverse direction compared to the beginning. Loading continues till the moment that the probe reaches the distance d. After this moment, the tissue enters into the slipping phase and the image again follows the probe with the same speed.

In Fig. 3 we demonstrate the actual result of a forward-backward 1 mm line scan in x-direction with a speed of 0.3 mm/sec. We observe that the position graph in x-direction (Fig. 3(c)) is very close to the ideal one described above. In this graph the thin line corresponds to the probe movement, the thick line corresponds to the image movement. We designate three different phases and determine them using three *rules-of-speed*.

1) **Slipping phase:** *The light (green) regions on the graphs correspond to the parts that the image closely follows the probe (the speed difference is less than 0.1 mm/sec).*

2) **Loading phase:** *The dark (black) regions correspond to the parts that the image speed is low (smaller than 0.1 mm/sec) although the speed of the probe is large (the difference is more than 0.1 mm/sec).* In these regions the tissue unloads and loads; therefore the image is almost stationary. The distances corresponding to this phase on the probe trajectory are designated as $2d_i$. This is because this distance can be expected to correspond to the double of the loading-distance designated in the ideal case of Fig. 2.

3) **Load+slip phase:** *The gray (pink) regions correspond to the parts that the image speed is not low (larger than 0.1 mm/sec) but is also not as high as that of the robot (the difference is more than 0.1 mm/sec).* Therefore, in these

regions there is partial loading and partial slipping occurring together. That is a phenomenon not noted in the finger slip studies. We name these parts as the load+slip phase of the scan. The distances corresponding to the load+slip phases in the probe trajectory are designated as g_i.

If the actual result in Fig. 3 corresponded exactly to the ideal case in Fig. 2, we could designate the loading-distance simply by taking the average of d_1 and d_2 values. However, the load+slip phenomenon observed in the actual case necessitates taking into account the partial loading in the start of every slipping. In the load+slip phases (pink/gray regions in Fig. 3), the image speed starts from a low value close to zero and linearly increases to a value close to the robot speed. Due to this linearity, we can assume that half of the distance covered in the load+slip phase corresponds to loading with almost zero image speed, and the other half corresponds to slipping with an image speed equal to that of the robot. Therefore we can assume that the load+slip phase of the scan contributes to the loading-distance with an amount of half of the distance covered by the robot in this phase, namely $g/2$.

Bringing together the contributions of the loading and load+slip phases, the loading-distance corresponding to the rules-of-speed can be calculated as follows:

$$d = \frac{d_1 + d_2}{2} + \frac{1}{2} \cdot \frac{g_1 + g_2}{2}$$

In the middle column of Table I, we present the loading-distance values calculated using the formula above, for varying speed and distance of scan for a sample beef liver tissue. The average loading-distance for this tissue is determined to be 0.191 mm with a standard deviation of 0.047 mm across all constant speed and constant distance experiments.

There is a difficulty with applying the rules-of-speed that it is not always possible to get a homogeneous distribution of the three different colors designating the three different regions. This is because the speed variation is not always smooth enough to automate the application of the rules-of-speed with the above formula. We propose approximating to the loading-distance by the difference between the peak-to-peak values of the probe and image trajectories in a line scan. In Fig. 3(b) one notices that the difference between the peak-to-peak distances of the two trajectories is almost constant throughout the scan. This difference, in fact, corresponds to the region traversed by the probe but not by the image. Therefore, it is closely related to the loading-distance of the tissue. The difference between the peak-to-peak distances can easily be determined considering a central period of the position signals. In the third column of Table I we present the differences between the peak-to-peak distances of the x-positions of probe and image trajectories. As it is observed, the average difference of the peak-to-peak measure is 0.205 mm, very close to the average loading-distance calculated by the rules-of-speed. The standard deviation, 0.051 mm is also close to that of the results with the rules-of-speed.

TABLE I
LOADING-DISTANCE VALUES CALCULATED WITH TWO DIFFERENT METHODS FOR A SAMPLE BEEF LIVER TISSUE

Constant Distance Line Scan (1 mm)		
	Loading-distance (mm)	
Scan speed (mm/sec)	Rules-of-speed (mm)	Difference of peak-to-peak (mm)
0.20	0.179	0.187
0.25	0.163	0.190
0.30	0.171	0.198
0.35	0.165	0.183
0.40	0.197	0.188
0.45	0.205	0.179
0.50	0.225	0.173
Average	**0.186**	**0.185**
Constant Speed Line Scan (0.30 mm/sec)		
	Loading-distance (mm)	
Scan distance (mm)	Rules-of-speed (mm)	Difference of peak-to-peak (mm)
0.50	0.136	0.140
0.75	0.154	0.188
1.00	0.172	0.192
1.25	0.190	0.235
1.50	0.193	0.244
1.75	0.334	0.356
2.00	0.190	0.213
Average	**0.196**	**0.224**
Overall		
Average	**0.191**	**0.205**
Std. deviation	0.047	0.051

In the following we propose a protocol for determination of the loading-distance based on the difference between the peak-to-peak distances. This protocol consists of a single forward-backward line scan lasting approximately 10 seconds. It is a calibration process that can be used in the start of any scan performance. The actual scan can afterwards be adapted to the determined loading-distance. This protocol simply takes the half of the difference between the distances covered by the probe and the image trajectories in one shot of the line scan.

Protocol for determination of the loading-distance:

1) Determine the speed of scan,

2) Make the robot drag the probe linearly with a distance of $d_r/2$; name the direction as the forward direction (forward direction is positive, backward direction is negative; d_r can typically be chosen 0.5 mm),

3) Start recording the position corresponding to the image motion,

4) Make the robot drag the probe linearly with a distance $d_r/2$ in the forward direction and d_r in the backward direction,

5) Stop recording the image motion,

6) Determine the minimum (p_{min}) and maximum (p_{max}) of the positions corresponding to the image motion,

7) The loading-distance is given by

$$d = \frac{d_r - (p_{max} - p_{min})}{2}$$

TABLE II
LOADING-DISTANCE VALUES FOR BEEF LIVER AND CHICKEN BREAST

Constant Distance Line Scan (1 mm)						
	Loading-distance (mm)					
Speed	Beef liver			Chicken breast		
(mm/sec)	A	B	C	A	B	C
0.20	0.157	0.108	0.156	0.161	0.174	0.219
0.25	0.117	0.099	0.157	0.141	0.157	0.197
0.30	0.134	0.098	0.156	0.169	0.138	0.199
0.35	0.153	0.132	0.162	0.182	0.144	0.151
0.40	0.150	0.126	0.155	0.190	0.141	0.155
0.45	0.124	0.107	0.144	0.149	0.158	0.207
0.50	0.117	0.075	0.141	0.160	0.136	0.218
Average	0.136	0.107	0.153	0.165	0.150	0.192
Average		*0,132*			*0,169*	
Std. dev.		*0,025*			*0,027*	

Constant Speed Line Scan (0.3 mm/sec)				
	Loading-distance (mm)			
Distance	Beef liver			Chicken breast
(mm)	A	B	C	
0.50	0.062	0.113	0.083	0.114
0.75	0.094	0.131	0.108	0.153
1.00	0.097	0.137	0.123	0.110
1.25	0.087	0.149	0.123	0.157
1.50	0.099	0.175	0.128	0.184
1.75	0.155	0.213	0.162	0.168
2.00	0.181	0.221	0.192	0.171
Average	0.111	0.162	0.131	0.151
Average		*0.135*		*0.151*
Std. dev.		*0.044*		*0.028*

Overall		
Average	**0.133**	**0.164**
Std. dev	0.035	0.028

IV. TESTS ON BEEF LIVER AND CHICKEN BREAST

In this section we perform loading-distance measurements with various scans on beef liver and chicken breast tissues. With these measurements we investigate the dependency of the loading-distance on the scan speed, scan distance and tissue type. The resulting loading-distance values are given in Table II and plotted in Fig. 4.

The loading-distance, d, depends on the friction between the soft tissue and the probe as well as the tissue structure. The friction depends on the pressure, but also on the hydration and the type of the tissue. In [24], it is demonstrated that the vertical force applied on soft tissue surface is proportional to the indentation depth. Throughout our experiments we maintain an indentation depth of 300±50 µm. We first bring the probe into contact with tissue in steps of 100 µm and then go further a distance of 300 µm. We determine the moment of contact by observing the images on the monitor. Based on [24] we can assume that we maintain a constant pressure across our different experiments. Before each experiment we hydrate the soft-tissue with a saline solution isotonic to blood. Therefore, we can assume a maximal hydration in the contact surface of all our experiments.

In [28], it is demonstrated that, in the case of finger, the friction force in the slipping phase slightly increases with increasing speed. This observation made us expect that the loading-distance, d, would increase with increasing speed. Fig. 4(a) depicts the loading-distance values with respect to

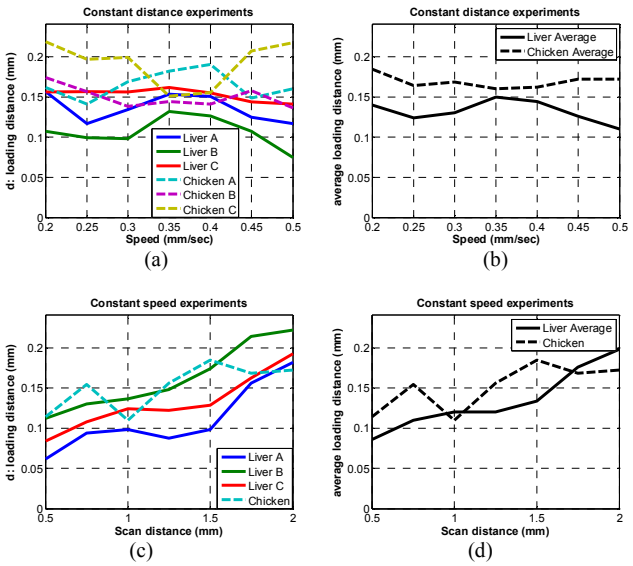

Fig. 4. Loading-distance values for various line scans on beef liver and chicken breast. (a) Constant distance (1 mm) line scans with different speed at three different locations (A, B, C) on each tissue; (b) average values of loading-distance for constant distance (1 mm) line scans with different speed; (c) constant speed (0.3 mm/sec) line scans with different scan distance at three different locations on beef liver (A, B, C) and single location on chicken breast; (d) average values of loading-distance for constant speed (0.3 mm/sec) line scans with different scan distance. In total loading-distance values of 70 different experiments are plotted.

scan speed on both beef liver and chicken breast tissues. In contrast to our expectations, the loading-distance remains almost constant across varying speed values with an average value of 0.132 (mm) and standard deviation of 0.025 for the beef liver and with an average value of 0.169 and standard deviation 0.027 for the chicken breast (Table II). Fig. 4(b) shows the average values separately for the beef liver and chicken breast. We observe that the average loading-distance for chicken breast is consistently larger than that of the beef liver across all speed values. This is expected since the chicken breast has a stickier surface compared to the beef liver.

Fig. 4(c) shows the dependency of the loading-distance on the scan distance with a constant speed of 0.3 mm/sec scan. We observe that the loading-distance slightly increases with increasing scan distance. On the other hand, the average values for varying scan distance are very close to those found for varying scan speed: 0.135 (mm) (compared to 0.132) with a standard deviation of 0.044 for beef liver and 0.151 (compared to 0.169) with a standard deviation of 0.028 for chicken breast. Based on the closeness of the averages, we can assume that the loading-distance remains almost constant for the given tissues. When we consider all speed and distance experiments, the average loading-distance is found to be 0.133 mm with a standard deviation of 0.035 mm for the beef liver and 0.164 mm with a standard deviation 0.028 mm for the chicken breast.

It should be noticed that the average loading-distance measured at different locations of the same piece of tissue slightly differs. This is probably because we did not maintain the same amount of pressure, although we followed

the same procedure to have the same amount of indentation. Another reason might be that there are slight differences of tissue structure at different locations. It should also be noticed that the average loading-distance for the beef liver used in the experiments of Table II (0.133 mm) significantly differs from that of the beef liver used in the experiments of Table I (0.205 mm). This observation points out that the loading-distance we measure might significantly differ across different pieces of the same type of tissue. The probable reason for this is that the pieces differed in shape and size.

Our results provide strong evidence that for a given piece of tissue, it is sufficient to determine the loading-distance at the start of any scan. Afterwards the measured value can be used throughout the scan. When the tissue is changed, the loading-distance should be determined anew. The results also suggest performing a new measurement each time the scan location is changed on the same piece. This means that the protocol we present is best to be used prior to each scan as a calibration procedure.

V. Application to a Square Scan

In this section we demonstrate the application of the loading-distance to perform a square scan on a beef liver tissue. We present the results of the experiment in Fig. 5.

If the knowledge of the loading-distance is not used and the robot is commanded to perform a square trajectory, the image trajectory will not be a proper square. This is illustrated in Fig. 5(a). The dark (black) line, representing the image trajectory, deviates from the light (green) line representing the probe trajectory. The deviation is most observed at the corners. The end point of the image trajectory is quite far from the start: the distance is more than 400 µm. The resulting mosaic is shown on the right hand side in Fig. 5(b).

In order to achieve a better square with the image trajectory we modify the probe trajectory by a length of the loading-distance at the corners of the square. For the experiment of Fig. 5(c) we command the robot with a loading-distance of 0.16 mm. The precision of the robot in following the commanded trajectory is up to 0.05 mm and the travel distance tends to be larger than what is commanded. Therefore, the realized loading-distance is around 0.20 mm.

The arrows in Fig. 5(c) indicate the compensation movement to unload the stress at the corners. When the probe reaches a corner, it translates further in the same direction by a loading-distance. After reaching the end of this distance, it translates in the reverse direction by the same amount and comes back to the target corner. At this moment the tissue is unloaded. The probe starts translating through the next perpendicular edge. Since the tissue is unloaded before starting each new edge, the image trajectory closely follows the probe trajectory. The improvement is clearly observed in Fig. 5(c). The probe trajectory closely follows the intended square. The distance between the start and end points is less than 100 µm. The corresponding mosaic in Fig. 5(d) is a much better square image compared to the one without the correction.

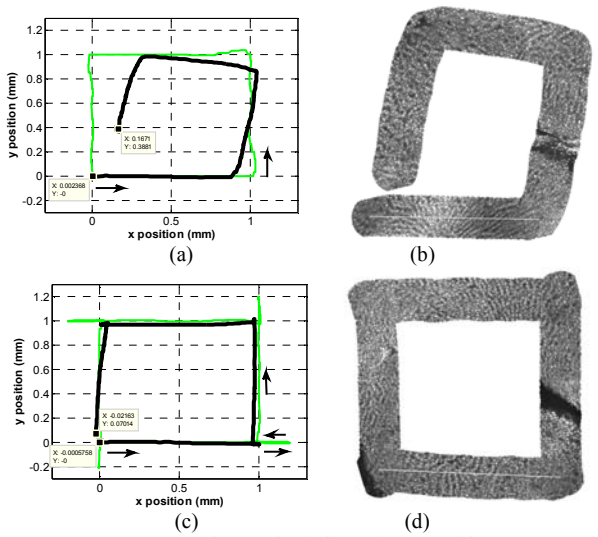

Fig. 5. Square scan results on beef liver tissue, with a commanded loading-distance of 0.16 mm (realized: 0.20 mm). (a) Square scan without unloading action; (b) image-mosaic corresponding to the square scan without unloading action; (c) square scan with unloading action; (d) image-mosaic corresponding to the square scan with unloading action. Light (green) lines: the probe trajectory; dark (black) lines: image trajectory.

VI. Conclusion

In this paper we present a first attempt to understand the behavior of soft tissue in surface contact with a hard object during microscopic scan. Our approach inspires from the load-slip phenomenon observed in slipping of a finger on hard surface. We apply the idea of load-slip to our soft tissue scan experiments and we come up with the parameter of loading-distance. This parameter describes the source of the deviation between the probe and image trajectories throughout the scan. We present in total 84 loading-distance measurements for line scan with varying speed and distance, on two different beef liver and one chicken breast pieces. Our results provide strong evidence that the loading-distance remains constant for a given location on the tissue during a single scan. We propose a protocol to measure the loading-distance. We demonstrate the effectiveness of using the loading-distance with a square scan experiment.

The loading-distance slightly varies in different locations of the same piece of tissue. The causes of this are not clearly identified with our experiments. We believe that the pressure applied on the tissue is the most important factor regarding these changes. In future work, we plan to equip our robot with a force sensor and perform loading-distance measurements with precise pressure recordings.

The loading-distance significantly varies across different pieces of the same type of tissue. The cause of this variation is expected to be the different shape and thickness of the pieces used. We plan to investigate the dependency of the loading-distance on the shape and thickness of the tissue placed under the probe. We consider that the change of the

loading-distance across different type of tissue (beef liver and chicken breast) is natural. The question is whether the loading-distance can be used as a characterizing parameter for the tissue structures, under specified pressure and for a specified shape. We would like to deepen our research in order to answer this question.

Although we used the proposed protocol for off-line measurement of the loading-distance, we did not yet implement it as an automated real-time measurement prior to an automated scan. In the future work we will perform this and integrate the measurement with the scan: the robot will automatically determine the loading-distance and perform the scan using this value at single shot of action. We will perform a full surface raster-scan with the correction action using the loading-distance, in such an automated manner.

We are further researching the systematic ways of using the knowledge of loading-distance to compensate any sort of movement on soft tissue, especially those following curved trajectories.

REFERENCES

[1] A.A. Tanbakuchi, J.A. Udovich, A.R. Rouse, K.D. Hatch, and A.F. Gmitro, "In vivo imaging of ovarian tissue using a novel confocal microlaparoscope," *American Journal of Obstetrics*, vol. 202, no. 1, pp. 90.e1-90.e9, 2010.

[2] V. De Sars, S. Haliyo, and J. Szewczyk, "A practical approach to the design and control of active endoscopes", *Mechatronics*, vol. 20, pp. 251-264, 2010.

[3] A.A. Tanbakuchi, A.R. Rouse, J.A. Udovich, K.D., Hatch, and A. Gmitro, "Clinical confocal microlaparoscope for real-time *in vivo* optical biopsies," *Jour. Of Biomedical Optics*, vol. 14, no. 4, pp. 044030.1-12, 2009.

[4] W. Piyawattanametha and T.D. Wang, "MEMS-based dual-axes confocal microendoscope," *IEEE Jour. Of Selected Topics in Quantum Electronics*, vol. 16, no. 4 pp. 804-814, 2010.

[5] E.J., Seibel, R.E. Carroll, J.A. Dominitz, R.S. Johnston, C.D. Melville, C.M. Lee, S.M. Seitz, and M.B. Kimmey, "Tethered capsule endoscopy, a low-cost and high-performance alternative technology for the screening of eshophageal cancer and Barrett's esophagus," *IEEE Trans. on Biomedical Engineering*, vol. 55, no. 3, pp. 1032-1042, 2008

[6] A.R. Rouse, A. Kano, J.A. Udovich, S.M. Kroto, and A.F. Gmitro, "Design and demonstration of a miniature catheter for confocal microendoscope," *Applied Optics*, vol. 43, no. 31, pp. 5763-5771, 2004.

[7] S.K. Chow, H. Hakozaki, D.L. Price, N.A.B. Maclean, T.J. Deerinck, J.C., Bouwer, M.E. Martone, S.T. Peltier, and M.H. Ellisman, "Automated microscopy system for mosaic acquisition and processing", *Journal of Microscopy*, vol. 222, pp. 76-84, 2006.

[8] V. Rankov, R.J Locke, R.J. Edens, P.R. Barber, and B. Vojnovic, "An algorithm for image stitching and blending", in *Proc. of SPIE*, vol. 5701, pp. 190-199, 2005.

[9] V. Becker, T. Vercauteren, C.H. von Weyhern, C. Prinz, R.M. Schmid, and A. Meining, "High-resolution miniprobe-based confocal microscopy in combination with video mosaicing," *Gastrointestinal Endoscopy*, vol. 66, no. 5, pp. 1001-1007, 2007.

[10] T. Vercauteren, A. Perchant, G. Malandain, X. Pennec, and N. Ayache, "Robust mosaicing with correction of motion distortions and tissue deformations for *in vivo* fibered microscopy," *Medical Image Analysis*, vol. 10, pp. 673-692, 2006.

[11] W. Piyawattanametha, H. Ra, M.J. Mandella, K. Loewke, T.D. Wang, G.S. Kino, O. Solgaard, and C.H. Contag, "3-D near-infrared fluorescence imaging using an MEMS-based miniature dual-axis confocal microscope", *IEEE Journ. of Selected Topics in Quantum Electronics*, vol. 15, no. 5, pp. 1344-1350, 2009.

[12] K.E. Loewke, D.B. Camarillo, W. Piyawattanametha, M.J. Mandella, C.H. Contag, S. Thrun, and J. K. Salisbury, "*In Vivo* micro-image mosaicing," *IEEE Trans. On Biomedical Engineering*, vol. 58, no. 1, pp. 159-171, 2011.

[13] E. Kobayashi, K. Masamune, I. Sakuma, and T. Dohi, "A wide-angle endoscope system using wedge prisms", in *MICCAI 2000, LNCS 1935*, Springer-Verlag pp. 662-668, 2000.

[14] B.C. Becker, R.A. MacLachlan, L.A.J. Lobes, and C.N. Riviere, "Semiautomated intraocular laser surgery using handheld instruments", *Lasers in Surgery and Medicine*, vol. 42, pp. 246-273, 2010.

[15] W.T. Latt, R.C. Newton, M. Visentini-Scarzanella, C.J. Payne, D.P. Noonan, J. Shang, and G.Z. Yang, "A hand-held instrument to maintain steady tissue contact during probe-based confocal laser endomicroscopy," *IEEE Tans. on Biomedical Engineering*, vol. 58, no. 9, pp. 2694-2703.

[16] M. Finke and A. Schweikard., "Motorization of a surgical microscope for intra-operative navigation and intuitive control", *The Int. Jour. Of Medical Robotics and Computer Assisted Surgery*, vol. 6, pp. 269-280, 2010.

[17] B. Rosa, B. Herman, J. Szewczyk, B. Gayet, and G. Morel, "Laparoscopic optical biopsies: in vivo robotized mosaicing with probe-based confocal endomicroscopy," *Proc. of IEEE/RSJ Int. Conf. on Intelligent Robots and Systems (IROS'2011)*, San Francisco, California, September 25-30, pp. 1339-1345, 2011.

[18] M. Baumhauer, M. Feuerstein, H.P. Meinzer, and J. Rassweiler; "Navigation in endoscopic soft tissue surgery – Perspectives and Limitations", *Journ. of Endourology*, vol. 22, no. 4, pp. 751-766, 2008.

[19] E.J. Seibel and Q.Y.J. Smithwick, "Unique features of optical scanning, single fiber endoscopy," *Lasers in Surgery and Medicine*, vol. 30, pp. 177-183, 2002.

[20] C.J. Engelbrecht, R.S. Johnston, E.J. Seibel, and F. Helmchen, "Ultra-compact fiber-optic two-photon microscope for functional fluorescence imaging *in vivo*," *Optics Express*, vol. 16, no. 8, pp. 5556-5564, 2008.

[21] G. Le Goualher, A. Perchant, M. Genet, C. Cave, B. Viellerobe, F. Berier, B. Abrat, and N. Ayache, "Towards optical biopsies with an integrated fibered confocal fluorescence microscope," in *Proc. IEEE Int. Conf. on Medical Image Computing and Computer-Assited Intervention –MICCAI 2004*, *Lecture Notes in Computer Science,* vol. 3217/2004, pp. 761-768, 2004.

[22] B.K. Tay, J. Kim, and M.A. Srinivasan, "*In vivo* mechanical behavior of intra-abdominal organs", *IEEE Trans. on Biomedical Eng.*, vol. 53, no. 11, pp. 2129-2138, 2006.

[23] Z. Gao, K. Lister, and J.P. Desai, "Constitutive modeling of liver tissue: experiment and theory", *Annals of Biomedical Engineering*, vol. 38, no. 2, pp. 505-516, 2010.

[24] X.P. Liu, S. Xu, H. Zhang, and L. Hu, "A new hybrid soft tissue model for visio-haptic simulation", *IEEE Trans. on Instrumentation and Measurement*, vol. 60, no. 11, PP. 3570-3581, 2011.

[25] K.M. Moerman, C.A. Holt, S.L. Evans, C.K.Simms, "Digital image correlation and finite element modeling as a method to determine mechanical properties of human soft tissue *in vivo*", *Journal of Biomechanics*, vol. 42, pp. 1150-1153, 2009.

[26] B. Qiao, G. Chen, X. Ye, "The research of soft tissue deformation based on mass-spring model", *Proc. of IEEE Int. Conf. on Mechatronics and Automation*, pp. 4655-4660, 2009.

[27] W. Ahn, H.S. Woo, J.Y. Kwon, J.K. Joo, and D.Y. Lee, "Model of frictional contact with soft tissue for colonoscopy simulator", *Proc. of IEEE Int. Conf. on Systems, Man and Cybernetics*, vol. 3, pp. 2714-2719, 2005.

[28] V.A. Ho and S. Hirai, "Understanding slip perception of soft fingertips by modeling and simulating stick-slip phenomenon", *Proc. of Robotics Science and Systems*, Los Angeles, CA, 2011.

[29] T. Andre, V. Levesque, V. Hayward, and P. Lefevre, "Effect of skin hydration on the dynamics of fingertip gripping contact", *Journ. of the Royal Society Interface*, doi: 10.1098/rsif.2011.0086, Published online, pp. 1-10.

[30] M. Tada, M. Mochimaru, and T. Kanade, "How does a fingertip slip? Visualizing partial slippage for modeling of contact mechanics", *Proc. of Eurohaptics 2006*, Paris, France, pp. 415-420, 2006.

[31] T. Vercauteren, A. Meining, F. Lacombe, and A. Perchant, "Real time autonomous video image registration for endomicroscopy: fighting the compromises," *Proc. of SPIE*, vol. 6861, pp. 68610C-68610C-8, 2008.